SCIENCE CHINA
Earth Sciences

• RESEARCH PAPER •

June 2017 Vol.60 No.6: 1159–1170
doi: 10.1007/s11430-016-9035-y

Comparison of paleotemperature reconstructions using microbial tetraether thermometers of the Chinese loess-paleosol sequence for the past 350000 years

TANG ChangYan, YANG Huan*, DANG XinYue & XIE ShuCheng

State Key Laboratory of Biogeology and Environmental Geology, School of Earth Sciences, China University of Geosciences, Wuhan 430074, China

Received January 7, 2017; accepted March 22, 2017; published online April 6, 2017

Abstract The recently proposed global and local calibrations for the mean annual air temperature (MAT) reconstruction on the basis of 5- and 6-methyl brGDGTs have rarely been applied to the Chinese LPS yet, leaving the applicability of these calibrations unclear. Here, we used the improved chromatography method to analyze 198 loess-paleosol samples from the Weinan section in the southern CLP for the past 350 kyr. The 6-methyl brGDGTs comprise a major proportion of total brGDGTs, pointing to alkaline conditions for most soil samples from the Weinan LPS. The decoupled profile variation of MBT'_{6ME} and MBT'_{5ME} suggests their response to different enviromental factors, possibly soil pH (or soil moisture) and temperature, respectively. This discrimination further corraborates that temperature and monsoonal precipitation were not in phase during the last four deglaciations on the CLP. Temperature estimates for the six calibrations tested show similar trends but remarkably differ in amplitudes. The soil moisture appears to affect the global MBT′/CBT calibration, the global MAT_{mr} calibration (a calibration based on the multiple linear regression) and the Chinese local SSM (Stepwise Selection Method) calibration, resulting in a significant underestimation of late Holocene temperature. In contrast, the dry climate has no effect on the global MBT'_{5ME} calibration. Of the six calibrations, only the Chinese local SSM calibration and global MAT_{mr} calibration produce temperature variation amplitude over the past 350 ka that is consistent with other independent proxy data. The recently proposed local calibrations based on 5- and 6-methyl brGDGTs for North China yield the amplitude of temperature changes that is much larger than the results determined by other approaches. All the six calibrations have their own weakness in the MAT reconstruction, due partly to the inconsistency between the brGDGT distribution in the Weinan LPS and the modern soils used to establish these calibrations.

Keywords 5-methyl brGDGTs, 6-methyl brGDGTs, Paleotemperature, Loess-paleosol sequences

Citation: Tang C Y, Yang H, Dang X Y, Xie S C. 2017. Comparison of paleotemperature reconstructions using microbial tetraether thermometers of the Chinese loess-paleosol sequence for the past 350000 years. Science China Earth Sciences, 60: 1159–1170, doi: 10.1007/s11430-016-9035-y

1. Introduction

The loess-paleosol sequences (LPS) in the Chinese Loess Plateau (CLP) have been proven to be good records of paleoclimatic changes during the Quaternary period (Heller and Liu, 1982; Liu and Ding, 1998; Ding et al., 2002). The interplay between the Asian summer and winter monsoon system (ASM and AWM) has been well documented by using a variety of geochemical and geophysical proxies, e.g., magnetic susceptibility (An et al., 1991; Fang et al., 1999; Maher et al., 1994), grain size (Ding et al., 1995) and the chemical weathering index (Ding et al., 1995; Guo et al., 1996). Although temperature and precipitation are climatic factors closely related to ASM in the CLP, modern meteorological monitoring reveals that the pattern and amplitude of variation in temperature and precipitation do not necessarily follow those of ASM (Liu et al., 2004). The (semi)quantitative reconstruction of temperature and

* Corresponding author (email: yhsailing@163.com)

precipitation independently are thus required to better understand the interaction between the climatic factors and their driving forces. On the basis of statistical relationship between proxies and temperature or precipitation for modern surface soils, the paleo-precipitation or paleo-temperature of CLP has been tentatively reconstructed by using proxies including magnetic susceptibility (Maher and Thompson, 1995; Porter et al., 2001), phytolith assemblages (Lü et al., 2007), cosmogenic ^{10}Be (Zhou et al., 2014) and organic carbon isotopes (Ning et al., 2008), etc.

The branched glycerol dialkyl glycerol tetraethers (brGDGTs) are also increasingly used tools for quantitative paleotemperature reconstruction in the LPS (Peterse et al., 2011, 2014). They are membrane lipids of some unknown bacteria that occur ubiquitously in terrestrial and marine environments (reviewed by Schouten et al., 2013). Their source bacteria are presumed to prefer a heterotrophic and anaerobic lifestyle (Weijers et al., 2004, 2009; Sinninghe Damsté et al., 2011). These lipids consist of two branched alkyl chains linked to two glycerol backbones via the ether bonds. The varying number of methyl and cyclopentyl moieties in the nine brGDGTs enables the development of MBT (methylation index of branched tetraethers) and CBT (cyclization of branched tetraethers) index, which qualify the relative number of methyl moiety and cyclopentyl rings, respectively (Weijers et al., 2007). MBT index is demonstrated to be mainly governed by mean annual temperature (MAT) and soil pH, whereas CBT only correlates with soil pH in global soils (Weijers et al., 2007). Due to the low abundance of brGDGT-IIIb and IIIc, these two compounds were excluded in the modified methylation index MBT′ (Peterse et al., 2012). The combination of MBT(′) and CBT, namely MBT(′)/CBT proxy, was widely used to reconstruct MAT and also soil pH in the LPS (Peterse et al., 2011; Gao et al., 2012; Zech et al., 2012; Jia et al., 2013), estuarine sediments (e.g. Sinninghe Damsté et al., 2012; Loomis et al., 2012) and peatlands (e.g. Weijers et al., 2011). Nevertheless, the global MBT′/CBT calibration produced significantly biased temperature estimates in semi-arid and arid regions because it appears that soil moisture and in turn MAP may impact both the MBT′ and CBT indices in the water-limited soils (Menges et al., 2014; Wang et al., 2014). A local MBT/CBT calibration, which was developed on the basis of brGDGT distribution in >100 Chinese soils covering a large climatic gradient, reduced the error in the temperature estimates, and later applied in the Weinan Holocene paleosol (Yang et al., 2014a, 2014b).

Recently, the original nine brGDGTs were found to harbor 1–3 isomers that exhibit different positions of methyl group (De Jonge et al., 2013). The 5- and 6-methyl brGDGTs, respresenting methyl at ω/α 5 and ω/α 6 position, respectively, show completely different response to pH and MAT (De Jonge et al., 2014b). MBT′$_{5ME}$, the methylation index after exclusion of 6-methyl brGDGTs, was found to be related only to MAT, whereas MBT′$_{6ME}$, the methylation index for 6-methyl brGDGTs, was pH-dependent (De Jonge et al., 2014a). Also, the relative abundance of 5- and 6-methyl brGDGTs is controlled primarily by soil pH (De Jonge et al., 2014a; Yang et al., 2015). The newly developed global MBT′$_{5ME}$ and MAT$_{mr}$ calibration for the MAT reconstruction can to some extent reduce the scatter in the original MBT′/CBT calibration, which may be partly caused by soil moisture (Peterse et al., 2014; Yang et al., 2014a; Wang et al., 2015). A recent study shows that the local calibrations based on 5- and 6-methyl brGDGTs for Northern China may improve the accuracy of temperature estimates compared to the global ones (Wang et al., 2016).

Until recently, almost all the paleo-reconstructions using brGDGTs in the LPS from the CLP have been performed based on the traditional nine brGDGTs, whose isomers generally co-eluted in the liquid chromatography (Peterse et al., 2011, 2014; Gao et al., 2012; Jia et al., 2013; Yang et al., 2014a). It has been widely demonstrated that separation of 5- and 6-methyl brGDGTs can markedly improve the accuracy of temperature and soil pH reconstruction in modern surface soils (De Jonge et al., 2014a; Ding et al., 2015; Xiao et al., 2015; Yang et al., 2015). However, the applicability of these isomer-based proxies and their pertinent calibrations to the Chinese LPS has not been thoroughly tested yet, despite the fact that Lu et al. (2016) has used the new chromatography method to separate 5- and 6-methyl brGDGTs and found some differences between traditional and new proxies in the Lantian LPS. Thus, we analyzed the 5- and 6-methyl brGDGTs in a LPS from Weinan in southwestern CLP using an improved liquid chromatography methodology and quatitatively reconstructed the paleotemperature variation over the last 350 kyr using different brGDGT-derived proxies and their pertinent calibrations. The results were compared to determine which proxy and calibration fit best for the paleotemperature in the southern CLP (Figure 1).

2. Materials and methods

2.1 Sampling

The Weinan LPS is located at the southeast part of CLP (Figure 2). Modern Weinan is mainly impacted by both ASM and AWM, resulting in a warm/humid summer and a cold/dry winter. The MAT and MAP averaged for 30 yrs (1961–1990) are 14.0°C and 575 mm, respectively (http://www.cma.gov.cn/). The Weinan section contains 34.8 m of LPS from L_4LL_1 loess (the topmost of L_4 phase corresponding to Marine Isotope Stage, MIS 10) to the Holocene paleosol S_0, and covers the last three glacial-interglacial

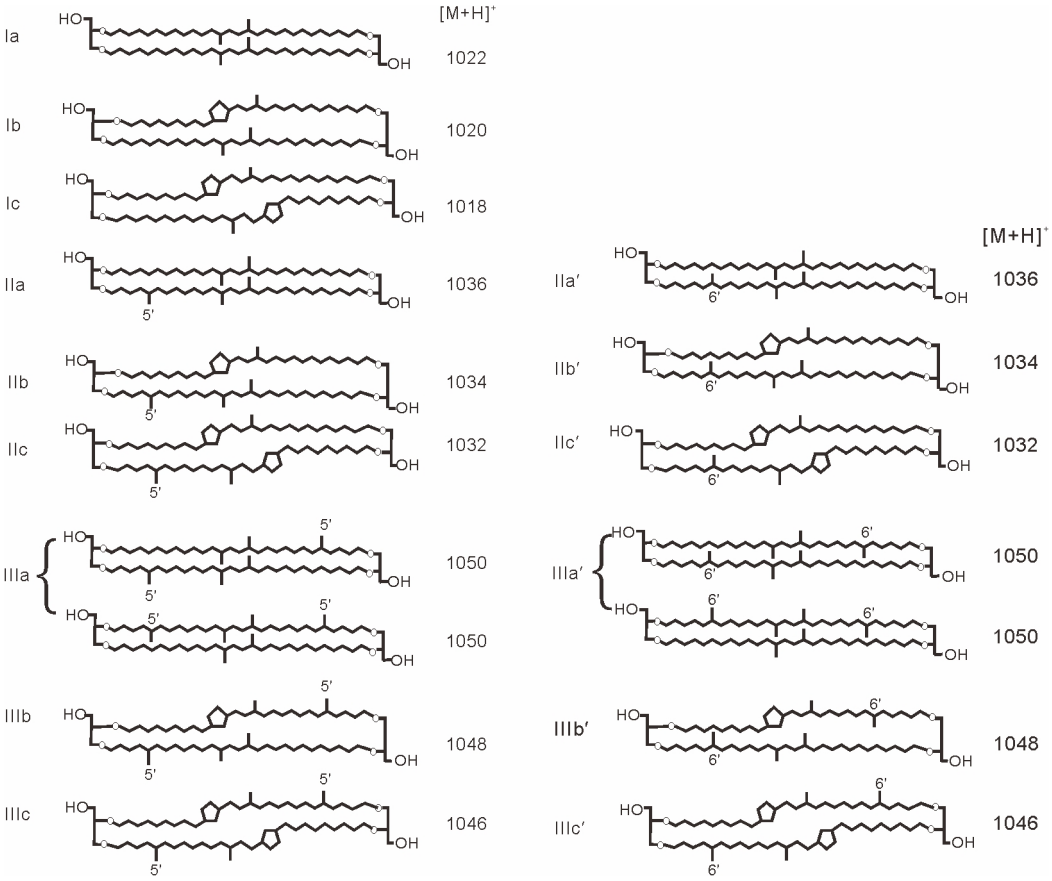

Figure 1 The structures of bacterial branched glycerol dialkyl glycerol tetraethers (brGDGTs).

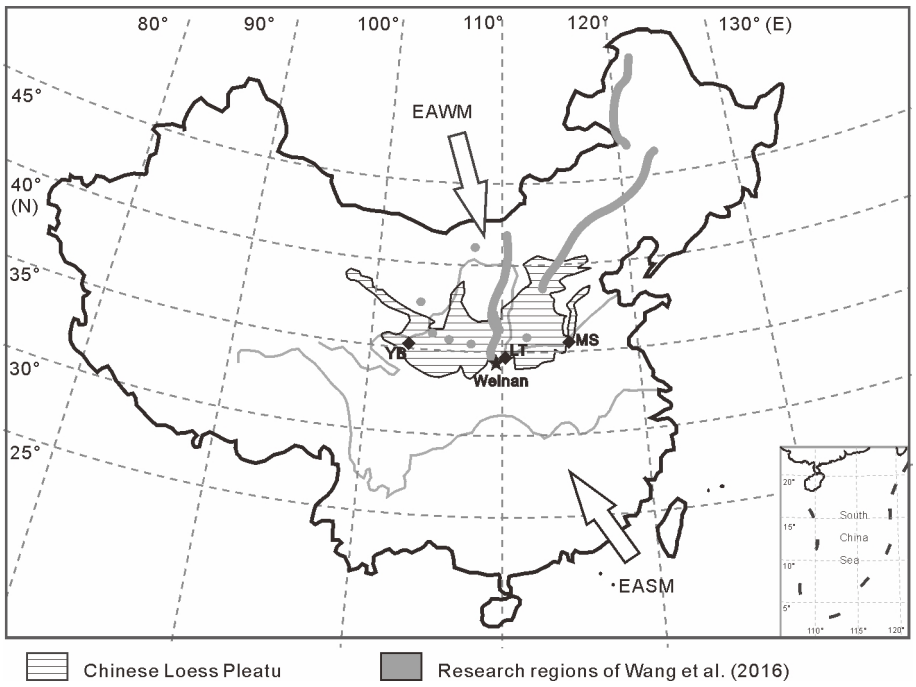

Figure 2 Chinese Loess Plateau and the sampling site in Weinan (black star). Black diamonds denote MS (Mangshan), LT (Lantian) and YB (Yuanbao) sections which used the MBT(′)/CBT proxy for the MAT reconstruction. The grey lines and spots represent the sampling regions for the North China soils reported by Wang et al. (2016). The arrows indicate the motions of the East Asia Summer Monsoon (EASM) and East Asia Winter Monsoon (EAWM), respectively.

cycles (MIS 1–9).

2.2 Magnetic susceptibility analysis and age model

The magnetic susceptibility was analyzed at 10 cm intervals, following the method described by Hao et al. (2012). The low-frequency magnetic susceptibility for a total of 349 samples was measured at 0.47 kHz using a Bartington Instrument MS 2B magnetic susceptibility meter.

The age model of the Weinan section was obtained by interpolation between geomagnetic polarity boundaries (Ding et al., 2002), using magnetic susceptibility as an indicator of accumulation rate (Kukla et al., 1988; Ding et al., 2002). This model is widely used to date the loess-paleosol sections of CLP (Bloemendal et al., 1995; Wu et al., 2001). The high correlation between magnetic susceptibility or grain size of loess/paleosol with benthic $\delta^{18}O$ records implies a strong coupling between the Asia summer/winter monsoon and ice volume changes (Ding et al., 1995, 2002; Hao et al., 2012), which allows to establish the chronology of Chinese LPS by correlation of mean grain size/magnetic susceptibility with the benthic $\delta^{18}O$ stack. Thus, ages of the glacial terminations and interglacial/glacial transitions inferred from the benthic $\delta^{18}O$ can be used as time controls for generating the loess chronology (Porter and An, 1995; Hao et al., 2012). In this study, the time controls reported by Ding et al. (2002) were used to determine the age model of the Weinan LPS. The data of magnetic susceptibility and grain size, analyzed at 10 cm intervals, represent an average time resolution of 0.3–2.6 kyr.

2.3 Lipid extraction

The loess-paleosol samples from Weinan were transported to the lab immediately after collection and dried in an oven at 45°C. A total of 198 samples were subjected to lipid extraction. Of them, 97 samples from 0–8.4 m depth, were collected from the last glacial loess (L1) and the Holocene paleosol (S_0) at 10 cm intervals. The remaining 101 samples from 8.4–34.8 m depth were collected at 40 cm interval.

Samples were ground into powder with a mortar and pestle and passed through a 20 mesh sieve to remove tiny roots and carbonate nodules. Each sample (40–50 g) was extracted with dichloromethane (DCM): Methanol (9:1, *v*/*v*) using an Accelerated Solvent Extractor (ASE 100, Dionex). The above extracts were concentrated via a rotary evaporator and then separated into apolar and polar fractions in a silica gel column by *n*-hexane and MeOH, respectively. All polar fractions containing GDGTs were passed through 0.45 μm polytetrafluoroethylene (PTFE) syringe filters and dried under a gentle stream of nitrogen gas.

2.4 GDGT analysis and proxy calculation

Each polar fraction was re-dissolved in 300 μL *n*-hexane: ethyl acetate (EtOA) (84:16, *v*/*v*), and spiked with a known amount of C_{46} glycerol trialkyl glycerol tetraether (GTGT), a synthesized internal standard (Huguet et al., 2006). An aliquot of each sample was injected and GDGTs were analyzed using an Agilent 1200 series liquid chromatography coupled to an Agilent 6460A triple quadruple mass spectrometry (LC-MS/MS). The separation of brGDGTs was achieved on two silica columns (150 mm×2.1 mm, 1.9 μm, Thermo Finnigan) in tandem. The elution gradients followed Yang et al. (2015). The selected ion monitoring (SIM) mode was used, monitoring *m/z* 1050, 1048, 1046, 1036, 1034, 1032, 1022, 1020, 1018 and 744, to improve the signal to noise ratio. The MS conditions followed Hopmans et al. (2004). The 6-methyl brGDGTs were denoted by an accent after the roman numerals for their corresponding 5-methyl isomers.

Several global or local calibrations for paleotemperature reconstruction have been proposed on the basis of the empirical relationship between brGDGT-derived proxies and temperature for the modern surface soils (Peterse et al., 2012; De Jonge et al., 2014b; Yang et al., 2014a; Wang et al., 2016). These calibrations were used to infer temperature in the Weinan LPS to determine which fits best for the LPS on the CLP. The temperatures proxies were calculated according to the calibration equations shown in Table 1. The Roman numerals in Table 1 refer to the corresponding GDGT structures shown in Figure 1.

Table 1 Definitions of GDGT indices

Index	Definition	Reference
MBT′	MBT′=(Ia+Ib+Ic)/(Ia+Ib+Ic+IIa+IIa′+IIb+IIb′+IIc+IIc′+IIIa+IIIa′)	Peterse et al. (2012)
CBT	CBT=−$\log_{10}$[(Ib+IIb+IIb′)/(Ia+IIa+IIa′)]	Peterse et al. (2012)
MBT'_{5ME}	MBT'_{5ME} = (Ia+Ib+Ic)/(Ia+Ib+Ic+IIa+IIb+IIc+IIIa)	De Jonge et al. (2014a)
MBT'_{6ME}	MBT'_{6ME} = (Ia+Ib+Ic)/(Ia+Ib+Ic+IIa′+IIb′+IIc′+IIIa′)	De Jonge et al. (2014a)
Index 1	Index 1 = log ((Ia+Ib+Ic+IIa′+IIIa′)/(Ic+Ia+IIc+IIIa+IIIa′))	De Jonge et al. (2014a)
IR_{6ME}	IR_{6ME}=∑(6-methylated brGDGTs)/∑(5-methylated brGDGTs+6-methylated brGDGTs)	De Jonge et al. (2014b)

2.5 Calculation of paleotemperature

Three global and three Chinese local brGDGT calibrations for the temperature reconstruction were tested. As brGDGTs were separated into 5- and 6-methyl components in this study, each of the original nine brGDGTs was calculated as a sum of all its isomers. Temperatures were calculated according to the six calibrations as follow.

The global MBT′/CBT calibration of Peterse et al. (2012):

$$\begin{aligned} &\mathrm{MAT} = 0.81 - 5.67 \times \mathrm{CBT} + 31.0 \times \mathrm{MBT}', \\ &n{=}176,\ R^2{=}0.59, \\ &\text{root mean standard error, RMSE } 5.0\,^\circ\mathrm{C}. \end{aligned} \quad (1)$$

The Chinese local calibration proposed by Yang et al. (2014a):

$$\begin{aligned} \mathrm{MAT} &= 20.9 - 13.4 \times [\mathrm{IIa}{+}\mathrm{IIa}'] - 17.2 \\ &\times [\mathrm{IIIa}{+}\mathrm{IIIa}'] - 17.5 \times [\mathrm{IIb}{+}\mathrm{IIb}'] {+} 11.2 \times [\mathrm{Ib}], \\ n &= 120,\ R^2 = 0.87,\ \mathrm{RMSE}\ 1.7\,^\circ\mathrm{C}. \end{aligned} \quad (2)$$

The above two equationsare developed on the basis of the traditional nine brGDGTs.

The global calibration of $\mathrm{MBT'_{5ME}}$ against MAT proposed by De Jonge et al. (2014a):

$$\begin{aligned} &\mathrm{MAT_{5ME}} = -8.57 + 31.45 \times \mathrm{MBT'_{5ME}}, \\ &n = 222,\ R^2 = 0.66,\ \mathrm{RMSE}\ 4.8\,^\circ\mathrm{C}. \end{aligned} \quad (3)$$

The multiple linear regression calibration based on the fractional abundances of 5- and 6-methyl brGDGTs (De Jonge et al., 2014a):

$$\begin{aligned} \mathrm{MAT_{mr}} &= 7.17 + 17.1 \times [\mathrm{Ia}] + 25.9 \times [\mathrm{Ib}] \\ &+ 34.4 \times [\mathrm{Ic}] - 28.6 \times [\mathrm{IIa}], \\ n &= 222,\ R^2 = 0.68,\ \mathrm{RMSE}\ 4.6\,^\circ\mathrm{C}, \end{aligned} \quad (4)$$

and two Chinese local calibrations recently proposed by Wang et al. (2016) based on the distribution of 5- and 6-methyl brGDGTs in 148 soils from the temperate northern China, covering a soil pH range of 4–9 and a MAT range of –5°C to 13°C:

$$\begin{aligned} &\mathrm{MAT} = 27.63 \times \mathrm{Index\ 1} - 5.72, \\ &n = 148,\ R^2 = 0.75,\ \mathrm{RMSE}\ 2.5\,^\circ\mathrm{C}, \end{aligned} \quad (5)$$

$$\begin{aligned} &\mathrm{T_{mr}}: \mathrm{MAT} = 18.84 \times [\mathrm{Ia}] + 42.44 \times [\mathrm{Ib}] \\ &- 149.68 \times [\mathrm{Ic}] - 52.00 \times [\mathrm{IIa}] + 6.36, \\ &n = 148,\ R^2 = 0.77,\ \mathrm{RMSE}\ 2.5\,^\circ\mathrm{C}. \end{aligned} \quad (6)$$

3. Results

3.1 BrGDGT distribution in the Weinan LPS

All the 5- and 6-methyl brGDGTs were detected in the Weinan LPS. As GDGT-IIIc and IIIc′ are generally below the detection limit in most samples, only 13 brGDGTs, including Ia, Ib, Ic, IIa, IIa′, IIb, IIb′, IIc, IIc′, IIIa, IIIa′, IIIb and IIIb′ were used for the data processing (Figure 3). GDGT-Ia, -Ib and -IIa′ collectively comprise 70% of total brGDGTs on average. Among them, brGDGT-Ia accounted for 17.8–46.5% of total brGDGTs, being the most abundant brGDGT component in general. The GDGT-IIIb concentration was quite low in most samples and even lower than the detection limit in some samples. The overall distribution of brGDGTs in loess layers was not significantly different from

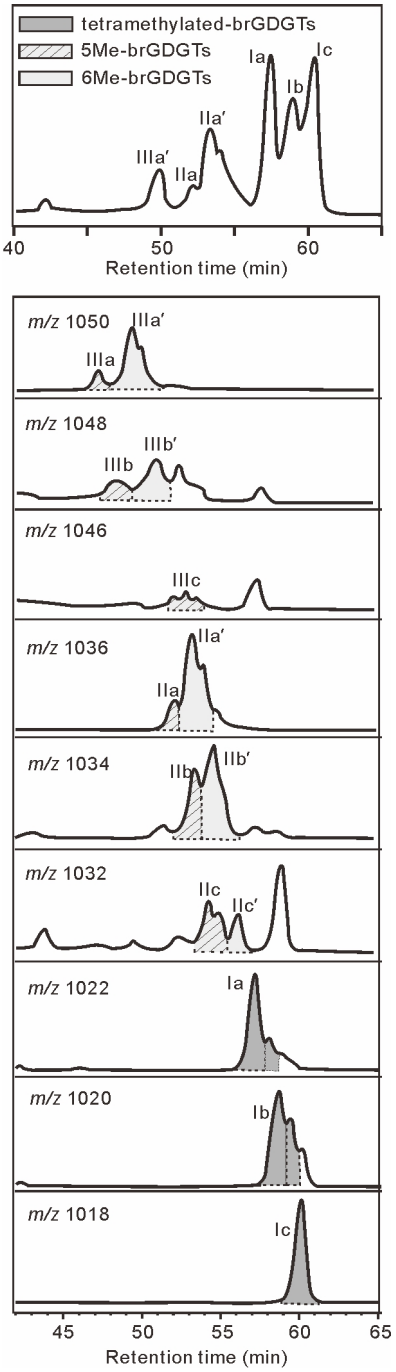

Figure 3 The separation of brGDGTs in a selected sample (10NJ-60) using two silica columns following the method described by Yang et al. (2015). The roman numerals refer to the structures in Figure 1.

that in paleosols. For example, the brGDGTs for S_0 and L_1 were both dominated by Ia and Ib, followed by pentamethylated IIa′ and IIb′. The 6-methyl brGDGTs exhibited a higher abundance than their 5-methyl isomers in both loess and paleosols, accounting for 34.6% of the total brGDGTs on average.

MBT′$_{5ME}$ and MBT′$_{6ME}$ showed similar variation tendency in most intervals of the past 350 kyr in the Weinan LPS. In the profile, MBT′$_{5ME}$ generally changes ahead of MBT′$_{6ME}$, but during some periods, e.g. ca 161.8–153.4 ka B.P. and 136.4–127.6 ka B.P. (Figure 4; highlighted grey bars), the variation of MBT′$_{5ME}$ and MBT′$_{6ME}$ exhibited an opposite trend.

3.2 Temperature reconstruction using different calibrations

3.2.1 Temperature reconstruction using the traditional nine brGDGTs

The MAT of the past 350 ka reconstructed from the global MBT′/CBT calibration (eq. (1)) ranged between 10.6°C and 22.7°C, with a value of 11.2°C for the topmost sample. The MAT produced from the Chinese local calibration (eq. (2)) varied from 13.2°C to 20.8°C, with a variation range of 7.6°C over the glacial-interglacial cycles. The maximum MAT (20.8°C) yielded by the eq. (2) occurred at the beginning of MIS 7, and was slightly higher than MAT for MIS 5, the penultimate interglacial. Furthermore, the eq. (2)-inferred MAT record revealed that the MIS 5c (ca. 113 ka B.P.) was the warmest within MIS 5, which was similar to the results of Lü et al. (2007) and Peterse et al. (2014). The minimum MATs yielded by the eqs. (1) and (2) both occurred at the late Holocene, with the temperature of 10.6°C and 13.2°C, respectively. The MATs reconstructed from the eqs. (1) and (2) generally exhibited similar values during glacial periods but differed significantly during the interglacial periods. The eq. (1)-derived MAT was ca. 2°C higher than the eq. (2)-derived one during the interglacial period (Figure 5b).

3.2.2 Temperature reconstructions using the 5- and 6-methyl brGDGTs

Although the eqs. (3) and (4) have similar RMSE in the reconstruction of MAT, the temperatures they produced dif-

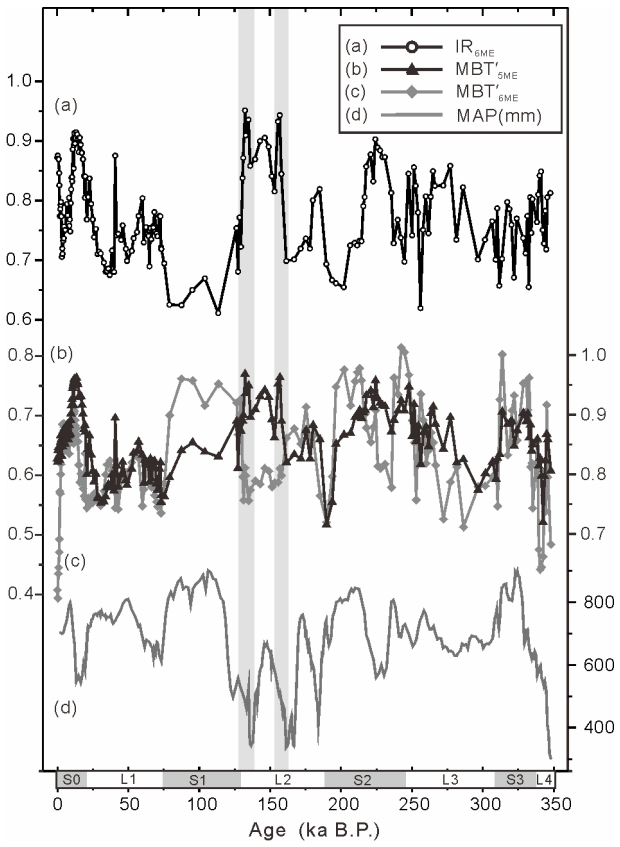

Figure 4 The variation of (a) IR_{6ME}, (b) MBT′$_{5ME}$, (c) MBT′$_{6ME}$ and (d) MAP reconstructed from magenetic suscepitibility using calibrations reported by Porter et al. (2001) in the Weinan section for the past 350 kyr. The grey bars highlight the periods when MBT′$_{5ME}$ and MBT′$_{6ME}$ show the opposite variation trend. The lithologic column shows the loess (light) and paleosol (dark), with S and L denoting paleosol and loess, respectively.

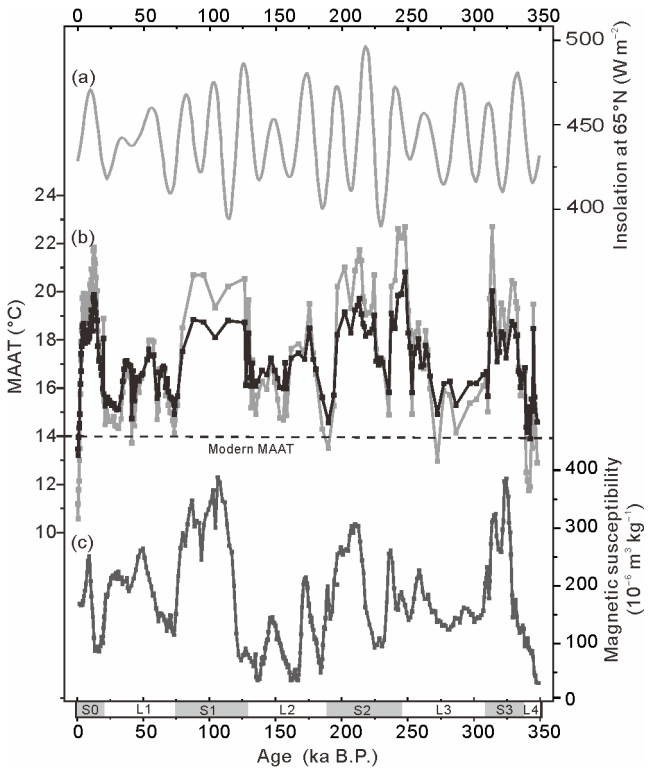

Figure 5 Comparison of the temperature variation over the past 350 kyr reconstructed from the traditional nine brGDGT-based calibrations with Northern Hemisphere insolation at 65°N and the magnetic susceptibility for the Weinan LPS; (a) Northern Hemisphere insolation at 65°N (Berger, 1978); MAT produced by (b) the MBT′/CBT calibration reported by Peterse et al. (2012) (grey curve) and by the Chinese SSM calibration reported by Yang et al. (2014) (black curve); (c) the magnetic susceptibility for the Weinan LPS.

fered remarkably in the Weinan LPS. The MBT′$_{5ME}$ calibration yielded temperatures that ranged from 13.9°C to 21.9°C and a MAT estimate for late Holocene (17.4°C) that was much higher than the modern MAT (14.0°C) (Figure 6b). The highest reconstructed MAT (21.9°C) was present in the upper part of L2 layer (MIS 7), corresponding to an age of ca. 131.1–158.3 ka B.P. (Table 2). It was even higher than the MAT estimates for the adjacent S1 layer (MIS 5), an interglacial period that has been generally considered to be the warmest over the last 350 ka (Petit et al., 1999; Kawamura et al., 2007). The lowest reconstructed MAT (13.9°C) occurred at 190 ka, which is the transitional period from S2 to L2 layer. In contrast, the MAT$_{mr}$ calibration (eq. (4)) yielded temperatures that showed a wider range (10.6°C) than that produced by the MBT′$_{5ME}$ calibration (eq. (3); 8.0°C). Similar to other reconstructions, the maximum MAT produced by the eq. (4) (23.7°C) also occurred at the beginning of MIS 7, and was also slightly higher than the MAT estimates for MIS 5. The minimum MAT (13.1°C) reconstructed from eq. (4) was present at the transition from L4 to S3 (Table 2).

The MAT produced by the eq. (5) ranged from 6.8°C for the boundary between L2 and S1 to 24.6°C for the Holocene maximum, with a total temperature range of 17.8°C (Figure 7). Similarly, the maximum MAT (22.1°C) inferred from the eq. (6) also occurred at the early Holocene and the minimum MAT (–10.3°C) at the transition from L2 to S1, with a large variation range of 32.4°C (Figure 7).

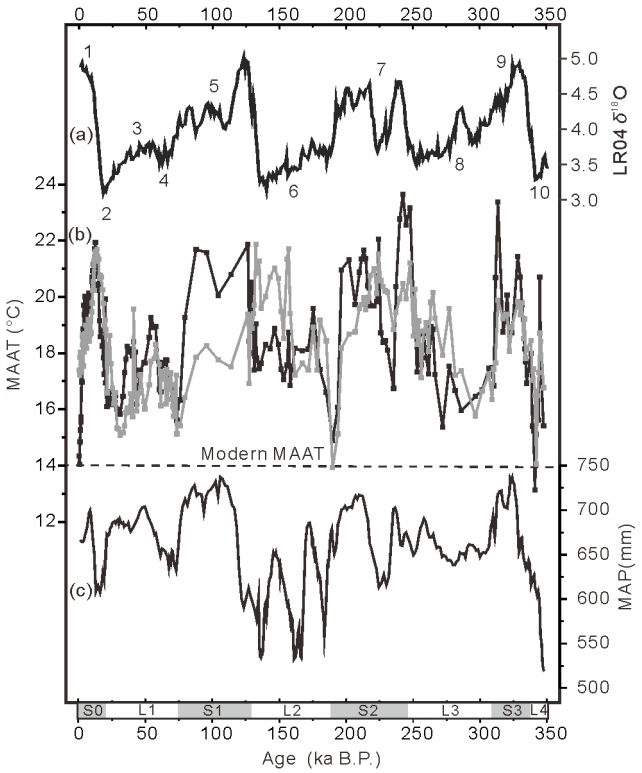

Figure 6 Comparison of temperature reconstructed from the calibrations based on 5- and 6-methyl brGDGTs with the magnetic susceptibility and the benthic foraminifera δ^{18}O. (a) The benthic foraminifera δ^{18}O stack (Lisiecki and Raymo, 2005); (b) MATs produced by the global MBT′$_{5ME}$ and MAT$_{mr}$ calibrations (the grey line and black line, respectively). The Arabic numerals 1-9 indicate the marine isotope stage (MIS); (c) MAP inferred from magnetic susceptibility for the Weinan section, using the calibration reported by Porter et al. (2001).

4. Discussion

4.1 Decoupled variation in MBT′$_{5ME}$ and MBT′$_{6ME}$

In comparison with MBT′$_{6ME}$, a considerable delay (up to 10 ka) was observed in the profile variation of MBT′$_{5ME}$ in the Weinan LPS over the past 350 ka. The decoupled pro-

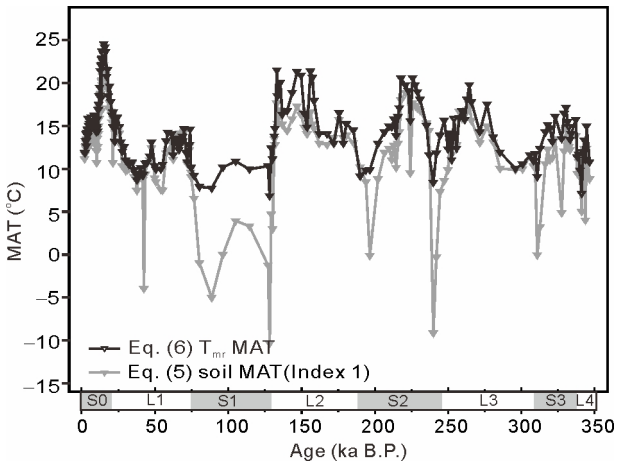

Figure 7 The temperatures reconstructed from the local calibrations based on 5- and 6-methyl brGDGTs (eq. (5), black triangle; eq. (6), grey triangle).

Table 2 The reconstructed temperatures using different calibrations for the Weinan LPS over the past 350 kyr

	Max MAT (°C)	Depth of max MAT (m)	Min MAT (°C)	Depth of min MAT (m)	MAT range (°C)	MAT for top S_0 (°C)
eq. (1)	22.7	30.4, S3	10.6	0.075, S0	12.1	11.2
eq. (2)	20.8	25.0, S2	13.2	0.075, S0	7.6	13.5
eq. (3)	21.9	12.7, S1	13.9	21.4, S2–L2	8.0	17.4
eq. (4)	23.7	24.6, S2	13.1	33.9, L4–S3	10.6	14.3
eq. (5)	24.6	2.125, S0	6.8	11.4, L2–S1	17.8	11.9
eq. (6)	22.1	2.125, S0	–10.3	11.4, L2–S1	32.4	11.2

file variation in MBT'_{6ME} and MBT'_{5ME} is more obvious in the past 80 kyr when sampling was conducted in a higher resolution. MBT'_{6ME} and MBT'_{5ME} essentially represent the relative abundance of 6- and 5-methyl brGDGTs vs. tetramethylated brGDGTs (Ia, Ib and Ic), respectively. Thus, the profile difference between MBT'_{6ME} and MBT'_{5ME} can be clearly visualised by the ratio of 6- vs. 5-methyl brGDGTs, namely IR_{6ME} index (Figure 4). The maximum IR_{6ME} value appears at the penultimate glaciation (ca. 126–152 ka B.P.), which is characterized by relatively high MBT'_{5ME} values and low MBT'_{6ME} values. Yang et al. (2015) noted that the difference between MBT'_{5ME} and MBT'_{6ME}, as well as the IR_{6ME} proxy, was both primarily controlled by soil pH in modern surface soils. The maximum IR_{6ME} values mean that the highest soil pH in the Weinan LPS and possibly the driest climate over the past 350 ka occur at the penultimate glaciation. This is consistent with the low northern hemispheric solar insolation at 65°N at this time interval, which was believed to be the major driving force of temperature and precipitation on the CLP (Peterse et al., 2011, 2014; Gao et al., 2012). As suggested by the high IR_{6ME} values (>0.9) at the penultimate glaciation, the 5-methyl brGDGTs only account for a small proportion of total brGDGTs; this might somewhat increase the error of MBT'_{5ME} calculation because unclear peaks for some 5-methyl brGDGT components in the chromatogram were observed during manual intergration (Figure 8). Thus, it cannot be fully ruled out that errors produced from the low abundance of 5-methyl brGDGTs may partly account for the abnormally higher MBT'_{5ME} at the penultimate glaciation.

The discrepancy in the profile trends between MBT'_{5ME} and MBT'_{6ME} throughout the LPS can be attributable to the different environmental variable(s) that they respond to. De Jonge et al. (2014a) and subsequent studies reveal that MBT'_{5ME} is strongly controlled by MAT while MBT'_{6ME} depends primarily on soil pH in humid and sub-humid regions (Yang et al., 2015). Further studies suggest that MBT'_{6ME} is mainly governed by the soil moisture in water-limited soils from semi-arid and arid regions (Dang et al., 2016; Wang et al., 2016). Thus, it is most likely that the MBT'_{5ME} and MBT'_{6ME} curves primarily reflect the variation of MAT and soil pH (or soil moisture), respectively. MAP has been generally thought to be the major environmental control on soil pH and soil moisture in monsoon-dominated region of China (Yang et al., 2014b). The variation of MBT'_{6ME} in the Weinan LPS may therefore indirectly reveals the change in monsoon precipitation. In fact, the decoupled variation in temperature and monsoonal precipitation has been also observed in other LPS, e.g., the Mangshan Section, Lantian Section and Yuanbao Section (Peterse et al., 2011, 2014; Gao et al., 2012; Jia et al., 2013), where the stalagmite $\delta^{18}O$ or magnetic susceptibility of loess-paleosol were used as proxies for monsoon precipitation (Maher and Thompson, 1995; Porter et al., 2001; Hu et al., 2008). However, due to a larger age uncertainty for the LPS than for the stalagmites, the lag time between temperature and monsoonal precipitation is difficult to be determined accurately in these LPS. As MBT'_{6ME} is positively correlated with soil moisture and in turn the MAP when IR_{6ME}>0.5 (Dang et al., 2016), it affords a novel approach to the reconstruction of MAP in the LPS. Currently, although the MAP cannot be reconstructed quantitatively using MBT'_{6ME} due to a lack of calibration, the variation trend of temperature and precipitation can be obtained by using MBT'_{5ME} and MBT'_{6ME}, respectively, which are both calculated from brGDGTs in the same section. The delay time between paleo-precipitation and paleotemperature can therefore be more precisely determined using only these two indices.

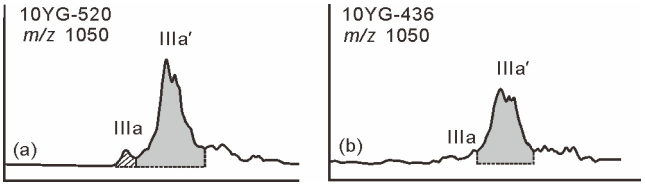

Figure 8 The normal (a) and unclear peaks (b) of brGDGT-IIIa.

4.2 Comparison of temperatures estimated by different calibrations

The temperature curves estimated by two calibrations based on traditional nine brGDGTs (eqs. (1) and (2)) exhbit the same trends and vary in phase with the Northern Hemisphere summer insolation at 65°N, suggesting the Northern Hemisphere summer insolation might be the major driving forcing of temperature variation in Weinan area. However, the two curves differ largely in amplitude (Figure 5b). The global MBT′/CBT calibration (eq. (1)) yields a wider amplitude (12.1°C) of temperature variation than the Chinese SSM calibration which produced a variation amplitude of 7.6°C (13.2°C to 20.8°C). The variation amplitude of the latter is more consistent with that reconstructed using phytolith assemblage in the same LPS (Lü et al., 2006, 2007). Moreover, the temperature (10.8°C) estimated for the topmost sample by the global MBT′/CBT calibration is much lower than the modern temperature (14.0°C). MAT reconstructed from the global MBT′/CBT calibration is overestimated for interglacial period but underestimated for the cold climate like late Holocene and the top layer of L4 loess (ca. 342.5–339.5 ka B.P.), consistent with our previous study for the Holocene (Yang et al., 2014a). This suggests that the local Chinese calibration have indeed improved the accuracy of paleotemperature reconstruction in the LPS.

After exclusion of 6-methyl brGDGTs, the calibrations based primarily on 5-methyl brGDGTs were believed to be more accurate in the reconstruction of MAT (De Jonge et al., 2014a; Ding et al., 2015; Yang et al., 2015). Compared to the result from the global MBT′/CBT calibration (eq. (1); 12.1°C), the global MBT'_{5ME} calibration (eq. (3)) indeed

yields a more reasonable amplitude (8.0°C) of temperature variation over the glacial-interglacial cycle. This amplitude is more consistent with that produced by the local Chinese SSM (Figure 5b) or reported by another study (Lü et al., 2007). The temperature estimate for late Holocene (17.4°C) is higher than the MAT of modern days in Weinan (14.0°C), possibly pointing to a bias towards the growing season air temperature. The MBT'_{5ME} calibration (eq. (3)) also produced some obviously unreliable temperature estimates. For example, the MBT'_{5ME}-inferred temperature shows that MIS 7 (the upper half L2 layer; ca.131.1–158.3 ka B.P.) is a period even warmer than the adjacent MIS 5 (S1 layer); the latter has been generally considered to be the warmest over the past 350 ka in other studies (Petit et al., 1999; Kawamura et al., 2007).

Although the eqs. (3) and (4) show similar RMSE, the temperatures reconstructed from them are different in the Weinan section. In addition to the difference in the temperature variation amplitude, the biggest differences between the two curves occur at the late Holocene and the transition period from MIS 6 to MIS 5 (the upper part of L2 to S1). The MAT_{mr} (eq. (4) produced a total temperature variation amplitude of 8°C for the Holocene, which is much higher than that determined by phytolith (Lü et al., 2007), and a temperature for the topmost soil that is close to modern MAT (14.0°C). However, closer inspection reveals that the temperature estimate is higher for the last glacial maximum (LGM; 20 ka B.P.) than for the late Holocene, a similar situation observed for the global MBT′/CBT calibration (eq. (1)) and the Chinese SSM calibration (eq. (2)). This is incosistent with the results from the climate modelling and other sedimentary archives, e.g., marine and lake sediments in the eastern Africa, which all show the LGM temperature is lower than modern temperature (De Villiers et al., 1995; Lea et al., 2000; Loomis et al., 2012). As noted earlier by Yang et al. (2014b), the present-day soils might be drier than the LGM soils, which was supported by a much higher $R_{i/b}$ value for the present than for the LGM in the Weinan LPS. Therefore, the soil aridity at late Holocene may to some extent influence the brGDGT calibrations, resulting in a lower temperature estimate for the present than for the LGM. As shown in Figure 4, the MBT'_{6ME} reaches its minimum value at late Holocene within the past 350 ka (<0.4); in contrast, the MBT'_{5ME} value is higher in modern days than in the LGM. This suggests that the low MBT'_{6ME} value was the main reason why the temperature was underestimated by the traditional MBT′/CBT calibration. Of the four calibrations discussed above, only the global MBT'_{5ME} calibration appears to be less affected by the soil moisture, yielding a higher temperature at late Holocene than at the LGM that accords with other studies (Lü et al., 2007). In fact, De Jonge et al. (2014a) also found that both the MBT′/CBT and MAT_{mr} calibrations underestimated the actual temperatures for a set of soils from relatively dry Iberian peninsula (100 mm<MAP<500 mm) and the impact of soil moisture on the latter calibration cannot be fully excluded although the latter has an improvement in the accuracy of temperature reconstruction compared to the former.

A wide range of studies have shown that local calibrations are generally considered to be better for paleoclimate reconstruction than global ones (e.g. Sinninghe Damsté et al., 2008; Bendle et al., 2010; Yang et al., 2014a). The local calibrations based on 5- and 6-methyl brGDGTs, i.e., eqs. (5) and (6), however, do not perform better in the MAT recontruction than the global ones. Although these two calibrations indeed produced temperatures for the topmost soils that are consistent with modern MAT, the variation amplitude of reconstructed MAT can reach up to 32.4°C for the four glacial-interglacial cylces, with the Holocene temperature fluctuation up to 15°C, which is obviously inconsitent with other studies (Lü et al., 2007). The glacial-interglacial cycles cannot be clearly identified according to the eq. (5) and 6-inferred MAT. For example, the temperature estimates were remarkably lower for S1 (MIS 5) than for the two neighouring loess layers L1 and L2. In fact, the soils used for the local calibrations (eqs. (5) and (6)) were collected primarily from the sites with a drier and colder modern climate than Weinan (Wang et al., 2016). The temperature reconstructed for most time intervals within the past 350 ka is higher than the modern MAT in Weinan, despite of the calibrations used. The range of temperature and soil humidity for Weinan over the past 350 ka is expected to be outside of those for the two local calibrations. Thus, the two local calibrations might be more applicable to the LPS in the Northern CLP.

To sum up, it appears that none of exsiting calibrations can produce temperatures that not only track the glacial-interglacial cyle but also agree well with other studies. This can be partly explained by that the abundance of brGDGT isomers in the Weinan section (Figure 9a) is remarkably different from that in either global soils or North China soils reported in previous studies (De Jonge et al., 2014a, Figure 9b; Wang et al., 2016, Figure 9c). The 6-methyl brGDGTs accout for a large fraction of total brGDGTs in soils from North China region (Wang et al., 2016) and Weinan LPS than in global soils (De Jonge et al., 2014a). The fractional abundance of IIa, a major component involved in many proxies, is only 3.6% on average in the Weinan LPS, in striking contrast with a mean value of 18% in the global soils. The brGDGT-IIa′ in North China soils shows the highest abundance within all brGDGTs, with a relatively lower abundance of tetramethylated brGDGTs (Ia, Ib and Ic), which is remarkably different from the brGDGT distribution pattern in the Weinan LPS. The different brGDGT distribution between the Weinan LPS and modern soils means that soils used for calibrations may not capture the environmental conditions when the LPS was developed. As the brGDGT distribution may be affected by

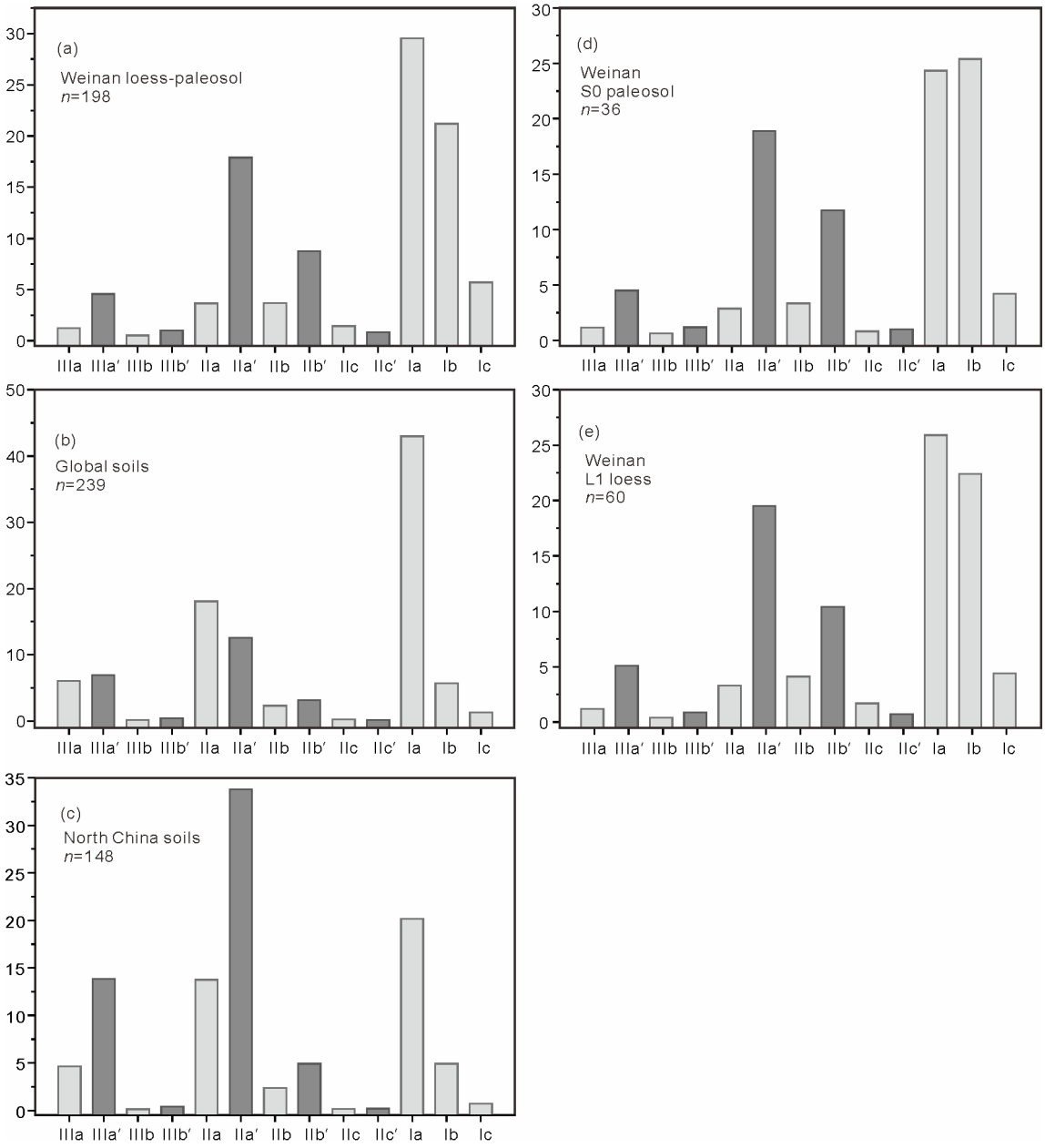

Figure 9 The histograms showing the fractional abundance of each brGDGT for (a) the Weinan LPS, (b) global surface soils reported by De Jonge et al. (2014a), (c) north China soils reported by Wang et al. (2016), (d) the Holocene paleosol in the Weinan LPS and (e) the L1 loess of the Weinan LPS. The dark bars highlight the 6-methyl brGDGTs and the light bars refer to the 5-methyl brGDGTs.

confounding factors including temperature, soil pH and soil moisture, the combined character of these three environmetal parameters for modern soils used for calibrations may be somewhat different from that for the LPS samples. Therefore, a local calibration covering a wider MAT and precipitation range is needed to better constrain the paleotemperature in the LPS.

5. Conclusion

The 5- and 6-methyl brGDGTs in a set of loess-paleosol samples for the past 350 kyr from the Weinan LPS were analzyed to test the applicability of exsiting brGDGT calibrations for the MAT reconstruction. The 6-methyl brGDGTs represent a major proportion of the total brGDGTs in the LPS and exert a significant impact on the original MBT′/CBT proxy particularly when climate is dry ($R_{i/b}$>0.5). A notable offset in the profile variation between MBT′$_{5ME}$ and MBT′$_{6ME}$ suggests a decoupled temperature and monsoonal precipitation during the last four deglaciations. The soil moisture or pecipitation may impact the global MBT′/CBT calibration, the Chinese local SSM calibration and the global MAT$_{mr}$ calibration, resulting in a lower temperature estimate for the present than for the LGM. Except the late Holocene dry period, the Chi-

nese local SSM calibration and the global MAT_{mr} calibration, which are based on the traditional nine brGDGTs and separated 5-/6-methyl brGDGTs, respectively, can both yield reasonable temperature range for the past 350 ka. However, the local calibrations based on 5-/6-methyl brGDGTs in North China soils produced temperature variation amplitude much larger than that determined by other approaches and should be used with caution in the southern CLP.

Acknowledgements *We sincerely thank the two anonymous reviewers for their insightful comments and suggestions, which are very valuable to our manuscript. Dr. Guoqiao Xiao, Gangqiang He and Long Ma are thanked for their help with the field work. This work was supported by the Key Research and Development Program of China (Grant No. 2016YFA0601100), the National Natural Science Foundation of China (Grant Nos. 41602189 & 41330103), the National Bureau for Foreign Experts and Ministry of Education of China (111 Project) (Grant No. B08030).*

References

An Z S, Kukla G J, Porter S C, Xiao J. 1991. Magnetic susceptibility evidence of monsoon variation on the Loess Plateau of central China during the last 130000 years. Quat Res, 36: 29–36

Bendle J A, Weijers J W H, Maslin M A, Sinninghe Damsté J S, Schouten S, Hopmans E C, Boot C S, Pancost R D. 2010. Major changes in glacial and Holocene terrestrial temperatures and sources of organic carbon recorded in the Amazon fan by tetraether lipids. Geochem Geophys Geosyst, 11: Q12007

Berger A L. 1978. Long-term variations of daily insolation and Quaternary climatic changes. J Atmos Sci, 35: 2362–2367

Bloemendal J, Liu X M, Rolph T C. 1995. Correlation of the magnetic susceptibility stratigraphy of Chinese loess and the marine oxygen isotope record: Chronological and palaeoclimatic implications. Earth Planet Sci Lett, 131: 371–380

Dang X Y, Yang H, Naafs B D A, Pancost R D, Xie S C. 2016. Evidence of moisture control on the methylation of branched glycerol dialkyl glycerol tetraethers in semi-arid and arid soils. Geochim Cosmochim Acta, 189: 24–36

De Jonge C, Hopmans E C, Stadnitskaia A, Rijpstra W I C, Hofland R, Tegelaar E, Sinninghe Damsté J S. 2013. Identification of novel penta- and hexamethylated branched glycerol dialkyl glycerol tetraethers in peat using HPLC-MS2, GC-MS and GC-SMB-MS. Org Geochem, 54: 78–82

De Jonge C, Hopmans E C, Zell C I, Kim J H, Schouten S, Sinninghe Damsté J S. 2014a. Occurrence and abundance of 6-methyl branched glycerol dialkyl glycerol tetraethers in soils: Implications for palaeoclimate reconstruction. Geochim Cosmochim Acta, 141: 97–112

De Jonge C, Stadnitskaia A, Hopmans E C, Cherkashov G, Fedotov A, Sinninghe Damsté J S. 2014b. *In situ* produced branched glycerol dialkyl glycerol tetraethers in suspended particulate matter from the Yenisei River, Eastern Siberia. Geochim Cosmochim Acta, 125: 476–491

de Villiers S, Nelson B K, Chivas A R. 1995. Biological controls on coral Sr/Ca and $\delta^{18}O$ reconstructions of sea surface temperatures. Science, 269: 1247–1249

Ding S, Xu Y, Wang Y, He Y, Hou J, Chen L, He J S. 2015. Distribution of branched glycerol dialkyl glycerol tetraethers in surface soils of the Qinghai-Tibetan Plateau: Implications of brGDGTs-based proxies in cold and dry regions. Biogeosciences, 12: 3141–3151

Ding Z L, Derbyshire E, Yang S L, Yu Z W, Xiong S F, Liu T S. 2002. Stacked 2.6-Ma grain size record from the Chinese loess based on five sections and correlation with the deep-sea $\delta^{18}O$ record. Paleoceanography, 17: 5-1–5-21

Ding Z L, Liu T S, Rutter N W, Yu Z W, Guo Z T, Zhu R X. 1995. Ice-volume forcing of East Asian winter monsoon variations in the past 800000 years. Quat Res, 44: 149–159

Fang X M, Ono Y, Fukusawa H, Bao-Tian P, Li J J, Dong-Hong G, Oi K, Tsukamoto S, Torii M, Mishima T. 1999. Asian summer monsoon instability during the past 60000 years: Magnetic susceptibility and pedogenic evidence from the western Chinese Loess Plateau. Earth Planet Sci Lett, 168: 219–232

Gao L, Nie J S, Clemens S, Liu W G, Sun J M, Zech R, Huang Y S. 2012. The importance of solar insolation on the temperature variations for the past 110 kyr on the Chinese Loess Plateau. Palaeogeogr Palaeoclimatol Palaeoecol, 317-318: 128–133

Guo Z, Liu T, Guiot J, Wu N, Lü H, Han J, Liu J, Gu Z. 1996. High frequency pulses of East Asian monsoon climate in the last two glaciations: Link with the North Atlantic. Clim Dyn, 12: 701–709

Hao Q, Wang L, Oldfield F, Peng S, Qin L, Song Y, Xu B, Qiao Y, Bloemendal J, Guo Z. 2012. Delayed build-up of Arctic ice sheets during 400000-year minima in insolation variability. Nature, 490: 393–396

Heller F, Liu T S. 1982. Magnetostratigraphical dating of loess deposits in China. Nature, 300: 431–433

Hopmans E C, Weijers J W H, Schefuß E, Herfort L, Sinninghe Damsté J S, Schouten S. 2004. A novel proxy for terrestrial organic matter in sediments based on branched and isoprenoid tetraether lipids. Earth Planet Sci Lett, 224: 107–116

Hu C Y, Henderson G M, Huang J H, Xie S C, Sun Y, Johnson K R. 2008. Quantification of Holocene Asian monsoon rainfall from spatially separated cave records. Earth Planet Sci Lett, 266: 221–232

Huguet C, Hopmans E C, Febo-Ayala W, Thompson D H, Sinninghe Damsté J S, Schouten S. 2006. An improved method to determine the absolute abundance of glycerol dibiphytanyl glycerol tetraether lipids. Org Geochem, 37: 1036–1041

Jia G D, Rao Z G, Zhang J Y, Li Z Y, Chen F H. 2013. Tetraether biomarker records from a loess-paleosol sequence in the western Chinese Loess Plateau. Front Microbiol, 4: 199

Kawamura K, Parrenin F, Lisiecki L, Uemura R, Vimeux F, Severinghaus J P, Hutterli M A, Nakazawa T, Aoki S, Jouzel J, Raymo M E, Matsumoto K, Nakata H, Motoyama H, Fujita S, Goto-Azuma K, Fujii Y, Watanabe O. 2007. Northern Hemisphere forcing of climatic cycles in Antarctica over the past 360000 years. Nature, 448: 912–916

Kukla G, Heller F, Ming L X, Chun X T, Sheng L T, Sheng A Z. 1988. Pleistocene climates in China dated by magnetic susceptibility. Geology, 16: 811–814

Lea D W, Pak D K, Spero H J. 2000. Climate impact of late Quaternary equatorial Pacific Sea surface temperature variations. Science, 289: 1719–1724

Lisiecki L E, Raymo M E. 2005. A Pliocene-Pleistocene stack of 57 globally distributed benthic $\delta^{18}O$ records. Paleoceanography, 20: PA1003

Liu C, Wang H, Jiang D. 2004. The configurable relationships between summer monsoon and precipitation over East Asia (in Chinese with English abstract). Chin J Atmos Sci, 28: 700–712

Liu T S, Ding Z L. 1998. Chinese loess and the paleomonsoon. Annu Rev Earth Planet Sci, 26: 111–145

Loomis S E, Russell J M, Ladd B, Street-Perrott F A, Sinninghe Damsté J S. 2012. Calibration and application of the branched GDGT temperature proxy on East African lake sediments. Earth Planet Sci Lett, 357-358: 277–288

Lu H X, Liu W G, Wang H Y, Wang Z. 2016. Variation in 6-methyl branched glycerol dialkyl glycerol tetraethers in Lantian loess-paleosol sequence and effect on paleotemperature reconstruction. Org Geochem, 100: 10–17

Lü H Y, Wu N Q, Yang X D, Jiang H, Liu K, Liu T S. 2006. Phytoliths as quantitative indicators for the reconstruction of past environmental conditions in China I: Phytolith-based transfer functions. Quat Sci Rev, 25: 945–959

Lü H Y, Wu N Q, Liu K B, Jiang H, Liu T S. 2007. Phytoliths as quantitative indicators for the reconstruction of past environmental conditions in China II: Palaeoenvironmental reconstruction in the Loess Plateau. Quat Sci Rev, 26: 759–772

Maher B A, Thompson R, Zhou L P. 1994. Spatial and temporal reconstructions of changes in the Asian palaeomonsoon: A new mineral magnetic approach. Earth Planet Sci Lett, 125: 461–471

Maher B A, Thompson R. 1995. Paleorainfall reconstructions from pedogenic magnetic susceptibility variations in the Chinese loess and paleosols. Quat Res, 44: 383–391

Menges J, Huguet C, Alcañiz J M, Fietz S, Sachse D, Rosell-Melé A. 2014. Influence of water availability in the distributions of branched glycerol dialkyl glycerol tetraether in soils of the Iberian Peninsula. Biogeosciences, 11: 2571–2581

Ning Y F, Liu W G, An Z S. 2008. A 130-ka reconstruction of precipitation on the Chinese Loess Plateau from organic carbon isotopes. Palaeogeogr Palaeoclimatol Palaeoecol, 270: 59–63

Peterse F, Martínez-García A, Zhou B, Beets C J, Prins M A, Zheng H, Eglinton T I. 2014. Molecular records of continental air temperature and monsoon precipitation variability in East Asia spanning the past 130000 years. Quat Sci Rev, 83: 76–82

Peterse F, van der Meer J, Schouten S, Weijers J W H, Fierer N, Jackson R B, Kim J H, Sinninghe Damsté J S. 2012. Revised calibration of the MBT-CBT paleotemperature proxy based on branched tetraether membrane lipids in surface soils. Geochim Cosmochim Acta, 96: 215–229

Peterse F, Prins M A, Beets C J, Troelstra S R, Zheng H, Gu Z, Schouten S, Damsté J S S. 2011. Decoupled warming and monsoon precipitation in East Asia over the last deglaciation. Earth Planet Sci Lett, 301: 256–264

Petit J R, Jouzel J, Raynaud D, Barkov N I, Barnola J M, Basile I, Bender M, Chappellaz J, Davis M, Delaygue G, Delmotte M, Kotlyakov V M, Legrand M, Lipenkov V Y, Lorius C, PÉpin L, Ritz C, Saltzman E, Stievenard M. 1999. Climate and atmospheric history of the past 420000 years from the Vostok ice core, Antarctica. Nature, 399: 429–436

Porter S C, An Z S. 1995. Correlation between climate events in the North Atlantic and China during the last glaciation. Nature, 375: 305–308

Porter S C, Hallet B, Wu X, An Z. 2001. Dependence of near-surface magnetic susceptibility on dust accumulation rate and precipitation on the Chinese Loess Plateau. Quat Res, 55: 271–283

Schouten S, Hopmans E C, Sinninghe Damsté J S. 2013. The organic geochemistry of glycerol dialkyl glycerol tetraether lipids: A review. Org Geochem, 54: 19–61

Sinninghe Damsté J S, Ossebaar J, Schouten S, Verschuren D. 2008. Altitudinal shifts in the branched tetraether lipid distribution in soil from Mt. Kilimanjaro (Tanzania): Implications for the MBT/CBT continental palaeothermometer. Org Geochem, 39: 1072–1076

Sinninghe Damsté J S, Ossebaar J, Schouten S, Verschuren D. 2012. Distribution of tetraether lipids in the 25-ka sedimentary record of Lake Challa: Extracting reliable TEX86 and MBT/CBT palaeotemperatures from an equatorial African lake. Quat Sci Rev, 50: 43–54

Sinninghe Damsté J S, Rijpstra W I C, Hopmans E C, Weijers J W H, Foesel B U, Overmann J, Dedysh S N. 2011. 13,16-Dimethyl Octacosanedioic Acid (iso-Diabolic Acid), a Common Membrane-Spanning Lipid of Acidobacteria Subdivisions 1 and 3. Appl Environ Microbiol, 77: 4147–4154

Wang H Y, Dong H L, Zhang C L, Jiang H C, Liu Z H, Zhao M X, Liu W G. 2015. Deglacial and Holocene archaeal lipid-inferred paleohydrology and paleotemperature history of Lake Qinghai, northeastern Qinghai-Tibetan Plateau. Quat Res, 83: 116–126

Wang H Y, Liu W G, Lu H X. 2016. Appraisal of branched glycerol dialkyl glycerol tetraether-based indices for North China. Org Geochem, 98: 118–130

Wang H Y, Liu W G, Zhang C L. 2014. Dependence of the cyclization of branched tetraethers on soil moisture in alkaline soils from arid-subhumid China: Implications for palaeorainfall reconstructions on the Chinese Loess Plateau. Biogeosciences, 11: 6755–6768

Weijers J W H, Schouten S, van der Linden M, van Geel B, Damsté J S S. 2004. Water table related variations in the abundance of intact archaeal membrane lipids in a Swedish peat bog. Fems Microbiol Lett, 239: 51–56

Weijers J W H, Schouten S, van den Donker J C, Hopmans E C, Sinninghe Damsté J S. 2007. Environmental controls on bacterial tetraether membrane lipid distribution in soils. Geochim Cosmochim Acta, 71: 703–713

Weijers J W H, Steinmann P, Hopmans E C, Schouten S, Sinninghe Damsté J S. 2011. Bacterial tetraether membrane lipids in peat and coal: Testing the MBT-CBT temperature proxy for climate reconstruction. Org Geochem, 42: 477–486

Weijers J W H, Panoto E, van Bleijswijk J, Schouten S, Rijpstra W I C, Balk M, Stams A J M, Damsté J S S. 2009. Constraints on the biological source(s) of the orphan branched tetraether membrane lipids. Geomicrobiol J, 26: 402–414

Wu N, Pei Y, Lu H, Rousseau D D. 2001. Orbital forcing of fast Asian summer and winter monsoon variations in the past 350 000 years (in Chinese with English abstract). Quat Sci, 21: 540–550

Xiao W J, Xu Y P, Ding S, Wang Y H, Zhang X Y, Yang H, Wang G A, Hou J Z. 2015. Global calibration of a novel, branched GDGT-based soil pH proxy. Org Geochem, 89-90: 56–60

Yang H, Lü X X, Ding W H, Lei Y Y, Dang X Y, Xie S C. 2015. The 6-methyl branched tetraethers significantly affect the performance of the methylation index (MBT′) in soils from an altitudinal transect at Mount Shennongjia. Org Geochem, 82: 42–53

Yang H, Pancost R D, Dang X Y, Zhou X Y, Evershed R P, Xiao G Q, Tang C Y, Gao L, Guo Z T, Xie S C. 2014a. Correlations between microbial tetraether lipids and environmental variables in Chinese soils: Optimizing the paleo-reconstructions in semi-arid and arid regions. Geochim Cosmochim Acta, 126: 49–69

Yang H, Pancost R D, Tang C Y, Ding W H, Dang X Y, Xie S C. 2014b. Distributions of isoprenoid and branched glycerol dialkanol diethers in Chinese surface soils and a loess-paleosol sequence: Implications for the degradation of tetraether lipids. Org Geochem, 66: 70–79

Zech M, Rass S, Buggle B, Löscher M, Zöller L. 2012. Reconstruction of the late Quaternary paleoenvironments of the Nussloch loess paleosol sequence, Germany, using *n*-alkane biomarkers. Quat Res, 78: 226–235

Zhou W J, Xian F, Du Y J, Kong X H, Wu Z K. 2014. The last 130 ka precipitation reconstruction from Chinese loess ^{10}Be. J Geophys Res-Solid Earth, 119: 191–197